Interatomic potentials for irradiation-induced defects in iron

Rebecca Alexander[a], Laurent Proville[a], Charlotte S. Becquart[b], Alexandra M. Goryeava[a], Julien Dérès[a], Clovis Lapointe[a], Mihai-Cosmin Marinica[a]

[a] *Université Paris-Saclay, CEA, Service de Recherches de Métallurgie Physique, 91191, Gif-sur-Yvette, France*

[b] *Université Lille, CNRS, INRA, ENSCL, UMR 8207 - UMET - Unité Matériaux et Transformations, F-59000 Lille, France*

Abstract

Empirical potentials using embedded atom method are developed for Fe, mainly to study irradiation-induced defects such as self-interstitial atom clusters or dislocation loops. The potentials are fitted using experimental values of solid-state properties, *ab initio* formation energies of basic point defects and *ab initio* forces acting on the atoms in the liquid or random state configurations. Various bulk and defect properties are compared to validate the transferability of the new potential. In this paper, we also investigate the energetic landscape of C15 self-interstitial atom clusters. In order to simplify and to facilitate the construction of lowest energy configurations in the complex energy landscape of C15 clusters, we test and propose three selection rules.

Keywords: Interatomic potentials, Embedded Atom Method , Fe, defects, screw dislocation, Molecular dynamics

1. Introduction

Materials of interest in the nuclear fission industry are the body centered cubic (bcc) metals, usually special steels with bcc iron base. Experimental and theoretical studies (1) have shown that the bcc lattice demonstrates improved radiation resistance compared to the close-packed face centered cubic lattice because of: (i) a reduced amount of vacancy and interstitial defect clustering and (ii) a higher stacking fault energy. Such features endorse continued development of ferritic/martensitic steels (2) as promising candidates for commercial nuclear reactor structures. As such, study of defects in Fe serves as the basis for future research regarding structural materials in the nuclear industry. It can also supplement the current industrial research and

Email address: mihai-cosmin.marinica@cea.fr (Mihai-Cosmin Marinica)

lead to better understanding of the behavior of structural materials exposed to radiation.

Radiation damage studies in Fe have posed a perplexing scenario for a while now due to the experimental observation of both $1/2\langle 111\rangle$ and $\langle 100\rangle$ families of SIAs depending on temperature (3; 4), unlike observations in other bcc metals (5). In addition, DFT provides theoretical evidence (6) for the existence of highly stable, small-sized three-dimensional SIA clusters with C15-type structure. In iron, the energy landscape of self-interstitial atoms organized in loops is relatively well known and has been widely investigated by various methods. However, the energy landscape of C15 clusters is very complicated due to an enormous number of possible configurations. Only a few recent studies investigate this problem(7; 8; 9; 10; 11; 12). The systematic exploration of the energy landscape with the goal of finding the minimum energy C15 configurations yields satisfactory results for small clusters (7; 8). Marinica et al. (6) used the Activation Relaxation Technique (13) for finding the lowest energy configurations for 2, 3 or 4 SIAs clusters. More advanced techniques using a genetic algorithm were proposed, making it possible to find the lowest energy configurations containing up to 10 SIAs (9). Using innovative algorithms Swinburne *et. al.* (14) proposed very efficient skim to bridge the energetic basins of the traditional dislocation loops and C15 clusters. Nonetheless, the number of possible configurations grow exponentially with the size of the cluster, making a systematic search prohibitive at larger sizes. This article intends to solve this problem in a more pragmatic approach by providing three *selection rules*, which are established from observations of the formation energies of several trial configurations, calculated using existing and newly-developed EAM potentials.

The purpose of the present article is to develop a potential for iron that includes the knowledge from the DFT scale of the energy landscape for C15 clusters (10). The motivation of such development is three-fold: (i) using theoretical means was stated that these clusters seem to nucleate at very small sizes and then dissociate into traditional loops. This observed mechanism seem to be in agreement with MD observations (15) and the *ab initio* energetic landscape (10). (ii) Moreover, using molecular dynamics simulations, is was stated that these three-dimensional C15 clusters can form under irradiations with only the Frenkel pair accumulation (11; 16) that mimics electron irradiation and not only in high-energy cascades as it was previously stated (6; 12). Moreover, the same studies pointed that the C15 clusters even precede production of loops under irradiation (11). (iii) The newly-developed potential is based on EAM formalism. This simple many-body radial force field enables numerical fast evaluation of millions of atoms opening the way to exhaustive exploration of the energetic landscape of C15 clusters up to clusters that contain hundreds of atoms. In this context, a reliable and numerical fast potential adapted to the investigation of energy landscape of C15 cluster and others irradiation defects, is crucial. This force field could helps to highlight the appropriate experimental conditions that

will enable the direct experimental evidence of the C15 clusters.

The paper is organized as follows: Section 2 discusses the existing empirical potentials for irradiation-induced defects in iron to emphasize the need for a new empirical potential. Section 3 focuses on the fitting strategy of existing empirical potentials in order to design the new empirical potentials. Section 4 briefly describes the fitting procedure adopted for the new Fe potentials and compares these new Fe potentials with the existing Fe potentials. To facilitate further studies, in section 5, the energy landscape of C15 clusters is discussed along with the three *selection rules* for the building of the most stable C15 cluster configurations for a given number of interstitials. The relative stability of the C15 clusters and dislocation loops is analyzed in the section 6. Finally, Section 7 presents our conclusions.

2. Existing traditional empirical potentials for defects in iron

Performance and transferability of empirical potentials are obviously related to the underlying physical model. Commonly used many-body interatomic models of metals have been derived from the second moment of tight binding approximation (17; 18; 19), EAM (20; 21) or Modified EAM (22) and higher order tight binding models (23; 24; 25; 26; 27; 28). Examples of different parametrizations for iron include a well known tight-binding second moment Finnis-Sinclair potential (29), the long range version given by Sutton and Chen (30) and the parametrization proposed in 1997 by Ackland et al. (31) (hereafter called A97). The force-matching method (32) was used to parametrize EAM potentials for defects in bcc metals such as iron and tungsten. Using the same fitting approach, Mendelev et al (33; 34) and Ackland et al (35) (A05) proposed a parametrization of iron. Using a different database (point defect oriented), Marinica (6; 36) (M10) obtained an improved parameterization for point defects. An empirical potential was developed to study thermally activated glide of dislocations (37), this potential will be denoted as P12. In the last decade, the empirical potentials based on machine learning approaches seem to be very promising (38; 39; 40; 41; 42; 43; 44; 45; 46; 47). However, these promising interatomic interactions, should be seen as interpolation of DFT calculations and not as standard empirical potentials. This approach fill the numerical gap between the traditional empirical methods and the DFT calculations. However, these machine learning potentials cannot replace the numerically fast empirical potentials that can easily treat millions of atoms over microseconds. This paper is restricted to numerically fast potentials, such as EAM or MEAM formalism. Moreover, we have limited the discussion to the most widely used iron potentials, in the last few years, namely A97, A05, M10 and P12 potentials.

Our main goal is to develop a potential, which gives reasonably accurate formation energy

values of C15 interstitial clusters relative to traditional planar clusters as well as for basic properties of extended defects, like dislocations. Hereafter, the SIA clusters will be denoted as I_n^{conf}, where n is the net number of SIAs, i.e. the number of additional atoms in the bcc lattice and $(conf)$ denotes a particular configuration of interstitial cluster. The morphology of small interstitial clusters has been widely studied in the past and it can be classified in two main classes: the parallel configurations formed by dumbbells packed together in bundles along $\langle 110 \rangle$ direction, $I_n^{\langle 110 \rangle}$, $\langle 111 \rangle$ direction, $I_n^{\langle 111 \rangle}$ or $\langle 100 \rangle$ direction, $I_n^{\langle 100 \rangle}$ and secondly, the non-parallel configurations where dumbbells are not aligned. Considering the most stable parallel configurations, the DFT calculations predicted that the orientation of these dumbbells changes from $\langle 110 \rangle$ to $\langle 111 \rangle$ above about five SIAs in Fe (6; 48). This holds for most empirical potentials except for the potentials fit prior to Mendelev 2003 EAM potential (33) and a few exceptions such as the $P12$ potential.

Some of the non-parallel configurations, called as self-trapped (49; 50), were observed for the first time in molecular dynamics simulation (49) using A05 potential. In the case of the di-interstitial we can recall the triangular self-trapped configuration, denoted hereafter as I_2^{gao} or $I_2^{triangle}$ (being first reported by Gao et al. in (51)): this instance has three atoms in interstitial positions and one vacancy sharing the same bcc lattice site (see Figure 1b). The reason why this configuration appears in high temperature MD simulation using A05 is due to very high vibrational entropy (50; 36). At 0 K the formation energy of I_2^{gao} is higher than the formation energy of $I_2^{\langle 110 \rangle}$, however the I_2^{gao} are stabilized by increasing the temperature (49; 50). The same trend is observed for bigger clusters for other self-trapped configurations, such as trians quadri- interstitials (see the geometry depicted in Figure 1e). Using DFT calculations (49; 36) the predicted formation energy of triangle configuration is found to be lower even than the parallel di-interstitial $I_2^{\langle 110 \rangle}$ (49). Moreover, the formation energy of self-trapped highly entropic non-parallel configurations, ring, tri- and tetra-interstitial configurations (Figure 1be) are very close to the formation energy of the parallel clusters. Systematic exploration of the energy landscape using an Eigenvector following method, ARTn by Marinica et al. (50) revealed a lot of non-parallel configurations and a very complex energy landscape of small interstitial clusters. Coupling this systematic search to lattice dynamics free energy calculations, Marinica et al. (6) were able to reach regions of phase space inaccessible by standard molecular techniques. Subsequently, they provided evidence for the C15 clusters (6). Moreover, using disconnectivity graph technique, they showed that in the case of I_4, the ring configuration shares the same energetic basin with the $3D$ C15 clusters. These C15 clusters can be seen as structures built with the non-parallel configurations. The building block of the C15 clusters is the di-interstitial configuration, I_2^{C15}, as seen in Fig. 1c. This I_2^{C15} can be visualized using 4 linked triangle configurations with each I_2^{gao} (depicted in Fig. 1b) having the central vacancy in the 4 corners

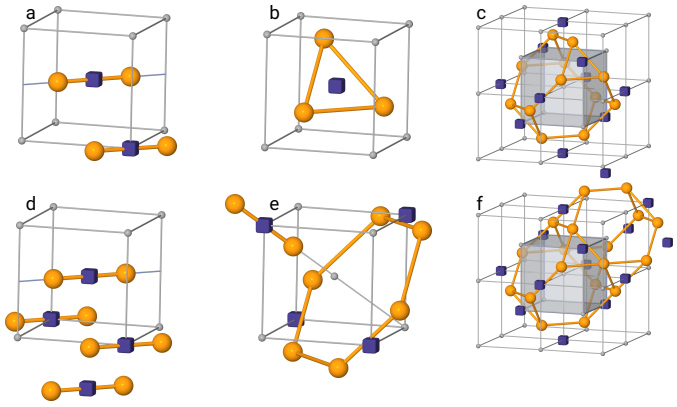

Figure 1: The configuration of di- and tetra-interstitial clusters in the (a,d) traditional ⟨110⟩ loop, (b,e) non-parallel and (c,f) C15 configurations. The atoms in interstitial position are marked by orange spheres and vacancies by blue cubes.

of the bcc cubic unit cell.

Figure 2 depicts the formation energies of the C15 clusters relative to the lowest energy of parallel dumbbell configurations (48; 6; 8) as a function of cluster size. The self-interstitial energy landscape provided by the P12 potential exhibits obvious anomalies making it unsuitable for point defect studies. The M10 potential follows rather well the DFT calculations, while the A05 or older A97 potential do not agree very well. Despite its weakness with respect to the point defect energy landscape, the Mendelev potentials (like A05) can serve as reference for the study of extended defects, such as screw dislocations in iron. Until 2012, the 2003 Mendelev potential was the only existing EAM potential in literature that successfully predicted the compact non-degenerate core of the screw dislocation in agreement with the *ab initio* calculation and the {110} glide plane of the screw dislocation in agreement with experiments and the *ab initio* calculations (37). However, all the Mendelev based potentials (33; 35; 34) exhibit two maxima for the Peierls barrier with a marked minimum mid-way, whereas *ab initio* calculations indicate only one maximum, as shown in Fig 3. The M10 potential, developed from the 2004 Ackland-Mendelev (A05) potential, gives very good energetics for point defects when compared with DFT calculations but the energy landscape of screw dislocation is not in agreement with DFT. The lowest energy configuration of the screw dislocation core is compact degenerate, whilst the Peierls barrier potential displays a lower energy configuration at the mid-way between the degenerate configurations. This situation is unphysical and needs to be corrected. The situation is inverse for the P12 potential: while the Peierls potential is improved and close to the *ab initio* calculations of Ventelon et al. (52), the point defect properties from the P12 potential have are poorly predicted. So far, each of the existing empirical potentials seem to have awkward characteristics, which prevents it from further use in studies of SIA clusters and screw dislocations in iron.

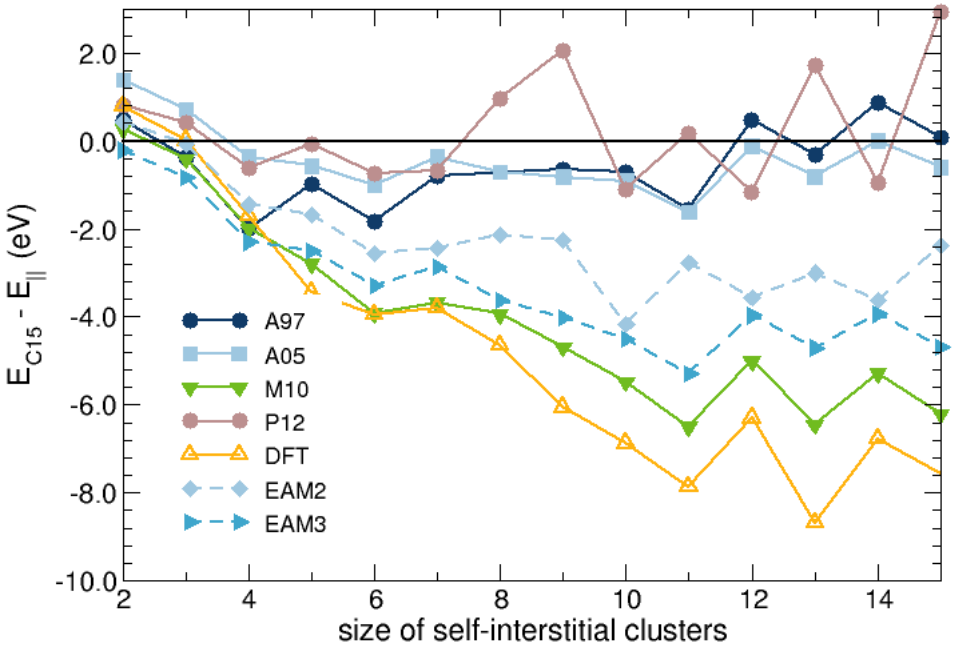

Figure 2: Formation energies of the C15 SIA clusters in bcc Fe calculated with respect to the lowest energy parallel-dumbbell configurations, i.e. with ⟨110⟩ orientation up to 4 SIAs and ⟨111⟩ orientation at larger sizes. The DFT results (10) are compared to those of selected empirical potentials and the newly-developed empirical potentials.

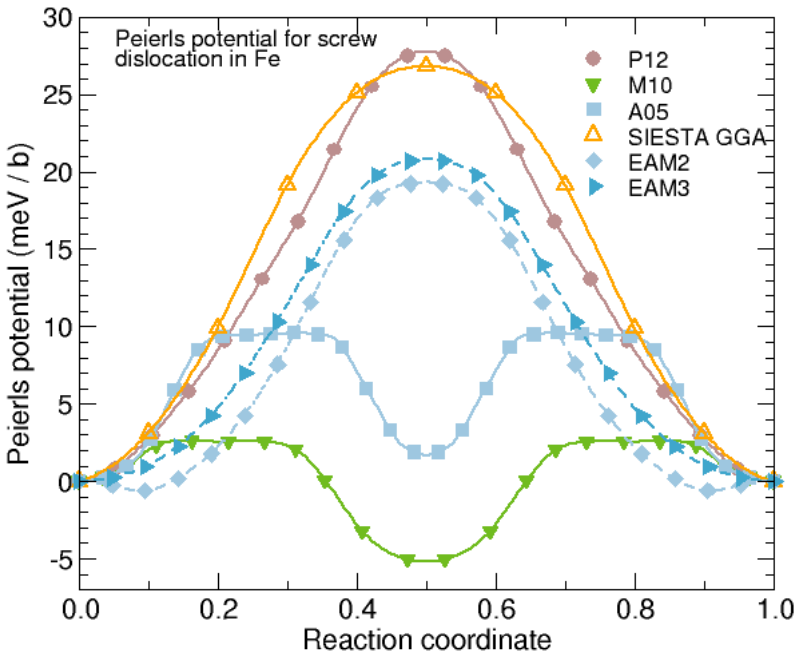

Figure 3: Comparison of Peierls barrier for selected existing potentials: SIESTA DFT-GGA (used as reference in this work) and the newly-developed empirical potentials.

In the following section, we discuss the fitting strategies adopted by the most widely-used empirical potentials and propose a strategy for fitting a new empirical potential for iron.

3. Lessons learned from evaluation of fitting strategy of existing interatomic potentials

The observables included in the database play a crucial role in the fitting. It is recommended to simulate properties that are close to those that were fitted. The most straightforward approach to fit the potential only on experimental observables of the crystal, such as: elastic constants, cohesive energy, Debye temperature etc. is insufficient. Some examples of different parametrizations for iron include a well known tight-binding second moment Finnis-Sinclair potential (29), the long range version given by Sutton and Chen (30) and the parametrization proposed in 1997 by Ackland et al. (31). Although these potentials fit bulk properties very well, they fail to reproduce simple properties of point defects such as the most stable configuration of the single interstitial. In iron, all these parametrizations predict $\langle 111 \rangle$ configuration to be the most stable instead of $\langle 110 \rangle$, as attested by DFT (53; 54; 48) and experiment (55). This contradiction is not surprising since the goal of any atomic potential is to represent the potential energy as a function of atomic coordinates by integrating electronic effects into a parametric form, which is determined by a fit. The environment of atoms in the $\langle 110 \rangle$ mono interstitial dumbbell is very different from the neighborhood of perfect bulk atoms: the length of the dumbbell is around 2.0 Å compared to 2.5 Å of the first nearest neighbor distance in bcc iron. Consequently, this change in the neighborhood results in a strong modification of the electronic density around interstitial atoms, which is also reflected in the drastically changing magnetism around the dumbbell. Such sharp effects cannot be caught by the physics injected in the tight binding second moment potentials. This lack of versatility of the physical model should be compensated by directly fitting a dumbbell environment.

More accurate potentials need to be developed using larger fitting data base that contain information beyond experimental quantities, e.g. the total energy or forces acting on atoms in various configurations provided by *ab initio* methods. The Force-Matching method proposed by Ercolessi and Adams in the late 90s (32) was used to parametrize EAM potentials suitable for modeling defects in bcc metals such as iron and tungsten: Mendelev et al (33; 34), Ackland et al (35) or Marinica et al. (6; 36) proposed a parametrization of iron. In 2005, Dudarev and Derlet designed an alternative approach (56) with a *magnetic* potential which was also based on the EAM formalism. By systematically enlarging the fitting database, these magnetic potential were continuously improved.

As pointed above, when using DFT calculations as benchmark, the C15 cluster energy landscape is more accurate predicted by M10 (36) potential compared to the A05 (35) potential. The main difference in the parametrization of the M10 (36) and the A05 (35) potentials is the database. The M10 potential is parametrized on a point defect related database including configurations of di-, tri- or tetra- interstitials provided by DFT calculations (48; 49). Among these configurations, Marinica et al.(36) also included the triangle configuration I^{gao}. In the procedure of fitting, only those parametrizations were selected for which the difference between the formation energy of the triangle configuration, I_2^{gao} (Fig. 1b) and the parallel dumbbell configuration, $I_2^{\langle 110\rangle}$ (Fig. 1a) is low. This approach did not succeed in attaining triangular configurations with lower energy but managed to considerably reduce the difference from 0.31 eV using A05 potential to 0.07 eV using M10 potential (see Table 1) (49; 36). Perhaps, this low formation energy of the triangular configuration, which serves as the building block for C15 clusters, influences the low formation energy of C15 clusters. In this new development, we will pay special attention to this triangular configuration.

4. Developing new potentials for iron

Overall, the main fitting procedure for developing new potentials in this work is similar to the one used for development of Fe (36) or W (57) potentials. As stated in (57), the database design has three components in order to produce suitable potential parametrizations for radiation defects: (i) experimental observables (elastic constants, cohesive energies, surface energies etc.), (ii) point defect related configurations and (iii) force matching method on the liquid or random iron configurations far from equilibrium. The details about the database are described in the Appendix (see 9.2). The parametrization is done using on-the-fly iterative minimization of cost function until the desired convergence is acquired (details are given also in (57)). Starting from the $P12$ potential, as an initial set of parameters, we have developed potentials for iron following the same three stages described in (57). The difference here is that we have selected only those parametrizations, from few hundreds of parametrizations, which resulted in a physical Peierls potential (single humped barriers) and low disparity in the formation energy of $I_2^{\langle 110\rangle}$ and I_2^{gao}.

Two of the developed potentials, hereafter called EAM2 and EAM3, give satisfactory results for most of the tests. Firstly, the bulk properties, such as the elastic constants, are improved compared to the starting $P12$ potential (Table 1). Secondly, the energy landscape of small interstitial clusters is improved. The relative energies of $\langle 110\rangle$ and $\langle 111\rangle$ mono-SIA configurations from the new potentials are in agreement with DFT studies (53; 54; 48). The $I_1^{\langle 110\rangle}$ is the most stable configuration, which is at variance with the predictions of the $P12$ and previous second moment or EAM potentials. Concerning di-interstitials, the difference between the formation

energy of $I_2^{\langle 110\rangle}$ and I_2^{gao} configurations is fairly reduced. Thirdly, as shown in Fig. 3, the Peierls barrier of the screw dislocation exhibits one single peak in qualitative agreement with the DFT calculations. However, it can be noted that obtaining improved energetic properties of the self-interstitials impact the quantitative agreement between DFT and the newly-developed potentials for the Peierls barrier. By comparison, the older $P12$ potential is found to be closer to DFT calculation than the new potentials. Nevertheless, the new potentials integrate more physics than the older $P12$ or $M10$ potentials.

Finally, the new potentials are tested for the relative stability of C15 clusters compared to the traditional clusters. As presented in Fig. 2, the new potentials exhibit reasonable agreement with the DFT calculations. Although these new potentials don't compare as well as the $M10$ potential, the energy landscape is acceptable and in the reasonable agreement compared to the previous parametrizations.

In the following section, we adopted a simplified representation of the C15 clusters and deduced three *selection rules* for construction of C15 configurations.

5. Construction of the stable C15 clusters

As mentioned earlier, the building block of the C15 family of SIA clusters is the cage-like di-interstitial I_2^{C15}, which is represented in Fig. 4(a-c). This di-interstitial I_2^{C15} is a Z16 Frank-Kasper polyhedron having 12 atoms at the interstitial positions together with 10 vacancies around a given bcc atomic site. Another Z16 polyhedron with 6 neighbours in common, can be constructed by adding 6 SIAs and 4 vacancies, resulting in a tetra-interstitial I_4^{C15}, which is represented by different visualizations in Figure 4(d-f). The two polyhedra have different orientations and are centered on two nearest neighbours of the bcc lattice. Similarly, larger C15 clusters can be constructed by addition of Z16 Frank-Kasper polyhedra having centers situated on a diamond network, which underlies the initial bcc structure. Other polyhedra can be progressively added to form clusters with 6, 8 and 10 SIAs, as illustrated in Figure 4(g-i), (j-l) and (m-o), respectively.

The centers of Z16 polyhedra form the diamond structure, whic can be obtained from the initial bcc lattice by removing half of atomic sites. This network is represented in Figure 4q. The final cubic unit cell of the constructed crystallographic structure is represented in Figure 4p and corresponds to the C15 Laves phase or the C15 structure of $MgCu_2$. In the mono-atomic Fe structure, interstitials occupy the Cu sites, half of the original bcc sites is empty and the second half is occupied and correspond to the Mg sites.

	Target	Potential				
		M10	A05	P12	EAM2	EAM3
Bulk Properties						
a_0 BCC (Å)	2.853	2.855	2.855	2.8148	2.831	2.835
a_0 FCC (Å)	3.6583	3.700	3.658	3.6569	3.658	3.662
E_{coh} BCC (eV/atom)	-4.28	-4.122	-4.013	-4.122	-4.123	-4.122
E_{coh} FCC (eV/atom)	-4.158	-4.000	-3.892	-4.000	-4.001	-4.000
C_{11} BCC (GPa)	243	243	243	226	243	243
C_{12} BCC (GPa)	145	145	145	150	145	145
C_{44} BCC (GPa)	116	116	116	115	116	116
Defect Properties						
$E_f^{\langle 111\rangle}$ (eV)	4.11	4.36	4.00	3.36	3.93	3.64
$E_f^{\langle 110\rangle}$ (eV)	3.41	3.69	3.53	3.75	3.45	3.37
$\Delta E_f^{I_2^{tri}-I_2^{<110>}}$ (eV)	-0.11	0.07	0.31	0.42	0.05	-0.01
$E_f^{V_1}$ (eV)	2.02	2.01	1.72	1.96	1.89	1.87
$E_b^{V_2}(1nn)$ (eV)	0.14	0.14	0.14	0.26	0.18	0.1
$E_b^{V_2}(2nn)$ (eV)	0.30	0.32	0.24	0.30	0.31	0.3
$E_b^{V_2}(3nn)$ (eV)	-0.02	-0.03	-0.03	-0.14	-0.03	-0.02

Table 1: Properties of bulk, mono- and di- interstitial and vacancies provided by some widely used potentials for iron: M10 (6; 36), A05 (35), the P12 (37) potentials, as well as the new EAM2 and EAM3 potentials. The target values are computed from the *ab initio* calculations, the same as those used for the development of the M10 and P12 potentials (36; 37). The a_0 and E_{coh} denote the lattice parameter and the cohesive energy, respectively. E_f and E_v are the formation energies of various orientation or configuration (the $1nn$, $2nn$ and $3nn$ denotes the first, second and third nearest-neighbor configurations of the di-vacancy). $\Delta E_f^{I_2^{tri}-I_2^{<110>}}$ is the difference between the formation energy of the di-interstitial triangle and $\langle 110\rangle$ configurations (positive/negative values indicate that $\langle 110\rangle$/triangle is the most stable.)

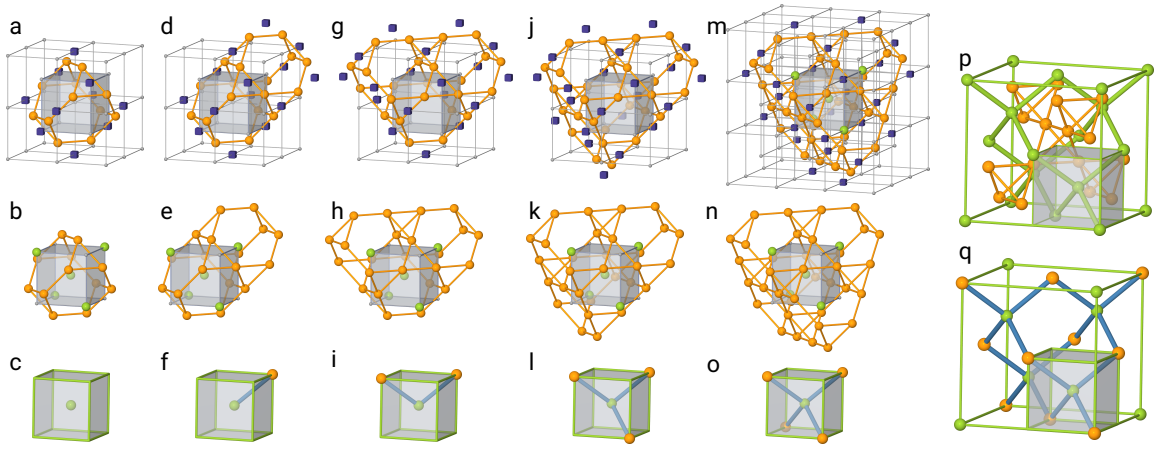

Figure 4: Structure of $I^{C15}_{2,4,5,8,10}$ clusters, in a bcc lattice in three different representations (a-o), the underlying diamond network of the centers of Z16 Frank-Kasper polyhedra (q) and the cubic unit cell of the C15 Laves phase $MgCu_2$ (p). The three equivalent representations of C15 clusters $I^{C15}_{2,4,5,8,10}$, respectively: (a,d,g,j,m) depict the positions of vacancies (blue cubes), atoms in interstitial positions (orange spheres) and the initial bcc lattice (grey atoms); (b,e,h,k,n) represent the sublattice built only by SIAs atoms, without the vacancies and the bcc lattice; (c,f,i,l,o) illustrate the positions of the corresponding Z16 polyhedra centers. The green and orange centers denote Z16 polyhedra that are different by a $\pi/2$ rotation. The blue bond denotes two nearest neighbour polyhedra. (q) The spheres in green and orange denote the possible locations of the Z16 polyhedra centers,which build the diamond structure. The plotted cube is the cubic unit cell of the original bcc lattice. (p) The unit cell of the cubic C15 Laves phase or $MgCu_2$, with the Mg atoms in green and the Cu atoms in orange. In our convention, the green and the orange atoms correspond to the centers of Z16 polyhedra and to the interstitial positions, respectively.

5.1. Selection rules for C15 construction

As stated earlier, the energy landscape of C15 clusters is not very well known and is very complicated due to an enormous number of possible configurations. The number of possible configurations of n SIA clusters in vaccuum (as metallic clusters, molecules, proteins) varies as $exp(n)$ (58). The situation is even more complicated for the SIA-clusters, which are embedded into bcc matrix, because the interaction between SIAs and the continuum of bcc states gives rise to many more configurations (50; 11; 12; 16; 14; 59). As a result, the full investigation of the energy landscape for large SIA-clusters (more than 10 interstitial atoms) is a herculean task. There is a need to develop a new strategy in order to search for the minima of C15 energetic basin. Our strategy is based by the generation of the C15 clusters using the diamond network formed by the centers of $Z16$ polyhedra. Similar to the configurations generated and represented in Fig. 4, larger clusters can be constructed. For the sake of simplicity, in subsequent figures we will depict only the atomic sites of the diamond network. In spite of this simplified representation, the number of possible configurations remains large. In order to limit these choices, after a careful study of the various C15 configurations and their corresponding formation energies, are proposed some *selection rules*.

Rule 1: the generated configurations will have the centers of $Z16$ *polyhaedra connected to its nearest neighbors on the diamond lattice.* This rule prevents the construction of configurations formed by two (or more) disconnected clusters, e.g. we eliminate those n SIA cluster configurations, which consist of two separate clusters of p and q self-interstitials atoms, where $p+q=n$. Let us take the case of I_4^{C15} that has two $Z16$ centers located in random lattice positions. According to this rule, only the configurations with centers in nearest neighbor position will be treated, which are depicted in Fig.4c). For the clusters with three $Z16$ centers, this rule leads to only one possible configuration depicted in Fig. 4i. All other possibilities will generate disconnected clusters and are ineligible.

In order to prevent the construction of open chains of $Z16$ centers, we impose the second rule that allows only those clusters that have a special topology. Let's take the example of I_{10}^{C15} presented in Fig. 5: many configurations are presented. All the EAM potentials confirm the same trend: the lowest energy configuration forms a closed ring with 5 $Z16$ centers. This observation leads to the second rule.

Rule 2: Closed hexagonal path made of 6 $Z16$ *centers are favored whenever possible.* The smallest structure having 6 Z16 connected centers is the I_{11}^{C15} cluster, which is shown in Fig. 6. Loop closure then occurs for specific sizes, referred to as magic numbers. After 11 interstitials, the next magic numbers are observed for I_{17}^{C15} and I_{23}^{C15} where two and three closed loops are

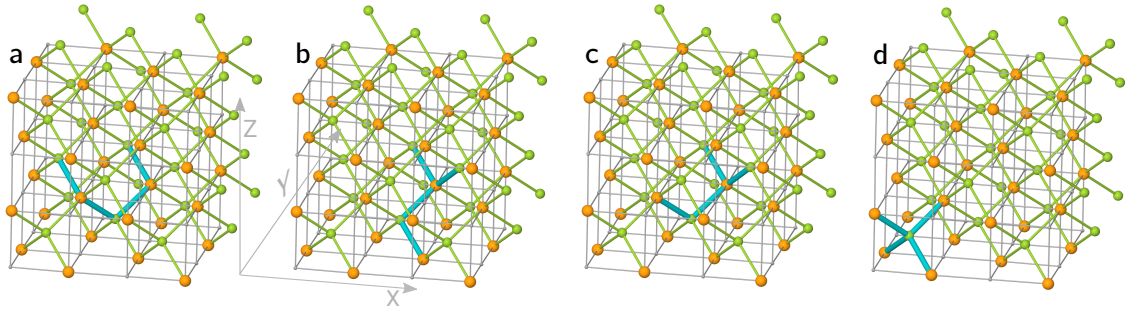

Figure 5: Four instances of I_{10}^{C15} cluster. The green and yellow spheres are the possible centers of $Z16$ polyhedra. The green centers correspond to the $Z16$ polyhedra rotated with 90 degrees around Z axis, with respect the polyhedra centered on yellow atomic sites. The blue bonds link the centers of trial configurations. The configuration (a) has the lowest formation energy for all three potentials M10, EAM2 and EAM3. The formation energy of (b), (c) and (d) configurations is higher for the potential (i) M10 with 1.15 eV, 1.41 eV and 1.70 eV, respectively (ii) EAM2 with 0.77 eV, 1.05 eV and 1.21 eV, respectively and (iii) EAM3 with 0.79 eV, 1.02 eV and 1.15 eV, respectively.

formed and packed in the most compact way possible. I_{17}^{C15} is presented in the Fig. 6. These structures indeed have very low formation energies.

The next step is to select, by formation energy criteria, the different possible constructions of clusters using the closed loop topology. Let's take the examples of the I_{17}^{C15} and I_{18}^{C15} clusters from Fig. 6. The I_{17}^{C15} cluster has a very compact $3D$ shape as opposed to the I_{18}^{C15} cluster, which is created by almost planar geometry of 2 closed loops. The two clusters have different number of interstitial atoms and conclusive interpretations can't be made. Therefore, different configurations of 22 interstitial atoms are used to compare energies of planar and compact $3D$ forms. The closed loops in compact form have lower formation energies as compared to closed loops in planar form. Hence:
Rule 3: the C15 clusters must be constructed in the most compact $3D$ *way respecting the first 2 rules.*

6. Relative stability of C15 clusters and dislocation loops

Design of reliable simulations requires precise knowledge of the energy landscape of interstitial defects. Here we compare the formation energies of the $1/2\langle 111\rangle$ dislocation loops and C15 clusters. Using the three *selection rules*, we have built and have computed the formation energy of C15 clusters up to hundreds of SIAs. Figure 7 depicts the formation energies of these two classes of defects employing different empirical potentials. All the presented potentials predict the crossover between the $1/2\langle 111\rangle$ and C15 clusters at sizes lower than 40 SIAs. The discrete

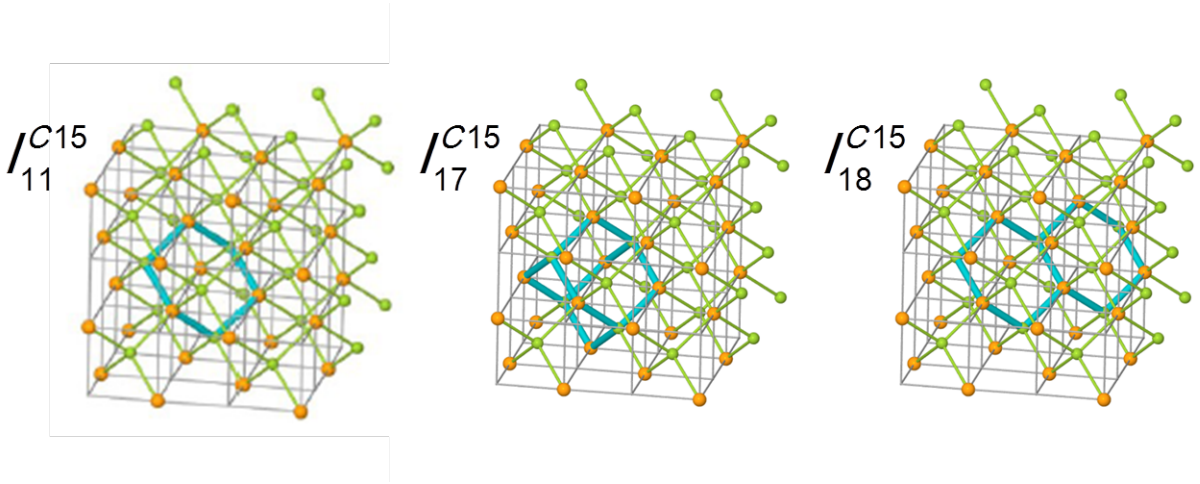

Figure 6: The configuration of I_{11}^{C15} and I_{17}^{C15} clusters, which are formed by one and three closed loops of Z16 centers, respectively. The I_{18}^{C15} cluster contains 2 plain closed loops yielding into a planar shape. The C15 clusters are represented using the same convention as in Fig5.

continuum model, which is based on accurate *ab initio* information, provides a crossover between 45 and 55 SIAs (10). Recently developed potential (16), using improved formalism, i.e. Analytical Bond Order potential, falls in the same range of predictions, as the present EAM potentials, by predicting a crossover around 25 SIAs. These empirical approaches give a good basis for description of the physics but the quantitative prediction are dependent on the potential. This characteristic remains even if great effort is made in order to fit a reliable set of parameters, as in the present development. When used in simulations, these inconsistent crossover values can result in conflicting predictions (16; 11; 6). For prediction of the crossover, the new potentials improve the performance of the AM05 potential but perform less accurate than the M10 potential. However, among the tested potentials, the newly developed potentials are the only ones that are also qualitatively good for modeling screw dislocations in iron.

7. Conclusions

In this article, we reviewed various empirical potentials based on EAM formalism that are used to study defects, such as dislocation loops or C15 clusters, in iron. We developed new empirical potentials for Fe, mainly adapted to study irradiation-induced defects, such as self-interstitial atom clusters or dislocation loops. These empirical potentials were developed using EAM formalism and are fitted on experimental values of solid-state properties, *ab initio* formation energies of basic point defects and *ab initio* forces acting on the atoms in the liquid or random state configurations. Various bulk and defect properties are compared to validate the transferability of the new potential.

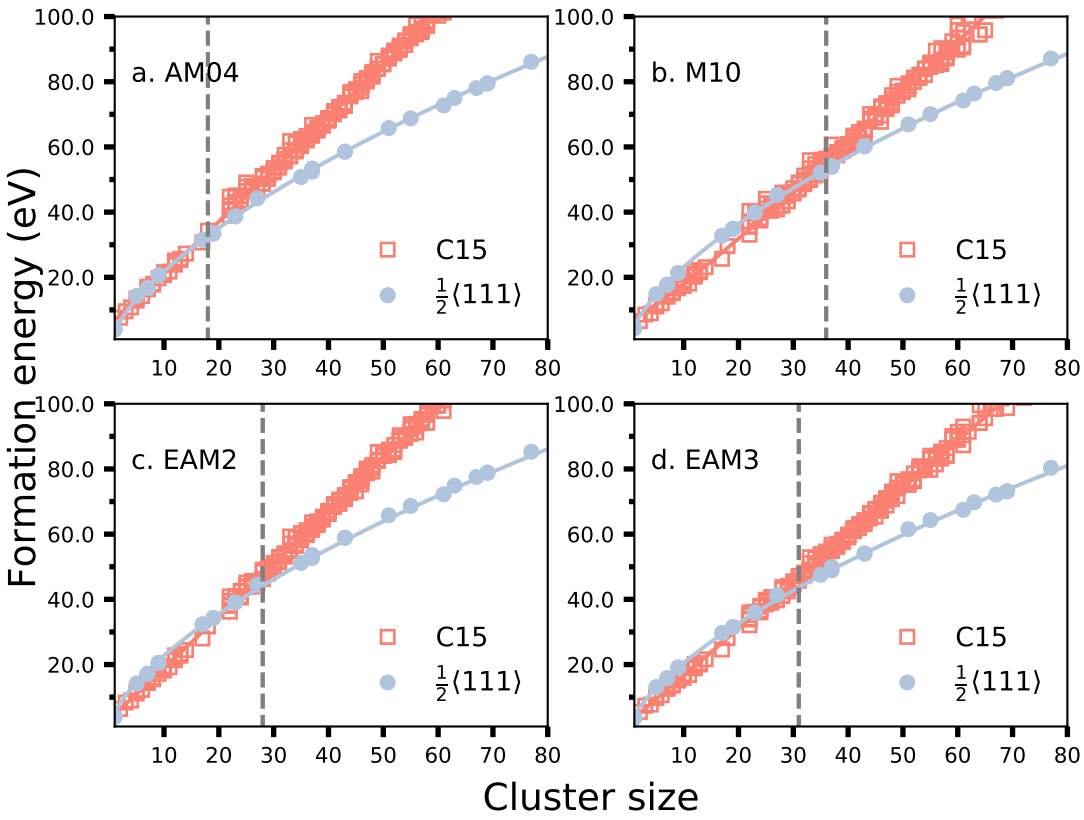

Figure 7: Formation energy of the $1/2\langle 111\rangle$ loops (full circles) and C15 clusters (empty squares) as a function of cluster size calculated using some selected potentials. The crossover between these two families of defects is emphasized by the vertical dashed line at the cluster size of 18, 36, 28, 31 SIAs for AM05, M10, EAM2, EAM3 potentials, respectively.

We have also explored the energy landscape of the three-dimensional C15 self-interstitial atom clusters using the present potentials and established three *selection rules* that facilitate the construction of lowest energy cluster configurations. These rules have practical importance enabling the construction of C15 clusters with hundreds of interstitial clusters with minimal effort.

The newly-developed potentials are used to address the relative stability of $1/2\langle 111\rangle$ dislocation loops and C15 clusters. This analysis gives a crossover between C15 and $\langle 111\rangle$ cluster below 50 SIAs. The crossover values are dependent on the empirical potential. The shortcomings of the existing Fe potentials highlight the lack of any universally applicable potential.

Ironically, even after additional developments and improvements, the traditional empirical potentials fail to reach a consensus on the energy landscape of radiation-induced defects in bcc metals. This provides us motivation to continue the development of new approaches in order to increase the accuracy and the transferability of empirical force fields, such as (i) the surrogate models (10) or (ii) recent machine / statistical learning approaches.

8. Acknowledgments

The authors acknowledge the support of the French Agence Nationale de la Recherche (ANR) under project project EPigRAPH ANR-14-CE07-0001. This work was financially supported by the Cross-Disciplinary Program on Numerical Simulation of CEA, the French Alternative Energies and Atomic Energy Commission. A.M.G., C.L., J.D. and M.C.M. acknowledge the support from GENCI - (CINES/CCRT) computer centre under Grant No. A0070906973. This work has been carried out within the framework of the EUROfusion Consortium and has received funding from the Euratom research and training programme 2014-2018 and 2019-2020 under grant agreement No 633053. The views and opinions expressed herein do not necessarily reflect those of the European Commission. This work also received funding from the Euratom research and training programme 2019-2020 under grant agreement No. 755039.

Table 2: Parameters of the empirical potential EAM2 for iron. The notations correspond to equations 1 - 4. Cubic spline knots are expressed in Å and coefficients of cubic polynomials for Φ and F in eV.

	EAM2	
a_1^Φ (δ_1^Φ)	-0.233077877775239D+01	(2.20)
a_2^Φ (δ_2^Φ)	-0.103581209869089D+02	(2.30)
a_3^Φ (δ_3^Φ)	0.428437254856161D+02	(2.40)
a_4^Φ (δ_4^Φ)	-0.349576674734256D+01	(2.50)
a_5^Φ (δ_5^Φ)	0.354802859068559D+01	(2.60)
a_6^Φ (δ_6^Φ)	-0.174365955103043D+01	(2.80)
a_7^Φ (δ_7^Φ)	0.117057813323836D+01	(3.00)
a_8^Φ (δ_8^Φ)	0.124837801738248D+01	(3.60)
a_9^Φ (δ_9^Φ)	-0.192553731845618D+01	(3.80)
a_{10}^Φ (δ_{10}^Φ)	0.187141961056927D+01	(4.20)
a_{11}^Φ (δ_{11}^Φ)	-0.132794059167828D+01	(4.40)
a_{12}^Φ (δ_{12}^Φ)	0.757518506386239D+00	(4.60)
a_{13}^Φ (δ_{13}^Φ)	-0.568818201964685D+00	(4.80)
a_{14}^Φ (δ_{14}^Φ)	0.117720442216161D+00	(5.20)
a_1^ρ (δ_1^ρ)	0.325300458437310D+03	(2.10)
a_2^ρ (δ_2^ρ)	0.139612614021368D+03	(2.40)
a_3^ρ (δ_3^ρ)	-0.466637825282012D+00	(3.20)
a_4^ρ (δ_4^ρ)	0.345546671885201D+00	(4.20)
a_5^ρ (δ_5^ρ)	0.152483050063800D-02	(5.00)
a_1^F	-1.000000000000000	
a_2^F	-0.746130823100000D-04	

Table 3: Parameters of the empirical potential EAM3 for iron. The notations correspond to equations 1 - 4. Cubic spline knots are expressed in Å and coefficients of cubic polynomials for Φ and F in eV.

	EAM3	
a_1^Φ (δ_1^Φ)	0.921517892958115D+01	(2.20)
a_2^Φ (δ_2^Φ)	-0.144798944569695D+02	(2.30)
a_3^Φ (δ_3^Φ)	0.431371044014217D+02	(2.40)
a_4^Φ (δ_4^Φ)	-0.257873824269047D+01	(2.50)
a_5^Φ (δ_5^Φ)	0.297073938005292D+01	(2.60)
a_6^Φ (δ_6^Φ)	-0.157691400786103D+01	(2.80)
a_7^Φ (δ_7^Φ)	0.114980279404543D+01	(3.00)
a_8^Φ (δ_8^Φ)	0.109124423545018D+01	(3.60)
a_9^Φ (δ_9^Φ)	-0.163540251149703D+01	(3.80)
a_{10}^Φ (δ_{10}^Φ)	0.120862772566493D+01	(4.20)
a_{11}^Φ (δ_{11}^Φ)	-0.551591685027562D+00	(4.40)
a_{12}^Φ (δ_{12}^Φ)	0.402688342667143D+00	(4.60)
a_{13}^Φ (δ_{13}^Φ)	-0.431736750904249D+00	(4.80)
a_{14}^Φ (δ_{14}^Φ)	0.756801011790600D-01	(5.20)
a_1^ρ (δ_1^ρ)	0.325300458437310D+03	(2.10
a_2^ρ (δ_2^ρ)	0.139612614021368D+03	(2.40)
a_3^ρ (δ_3^ρ)	-0.466637825282012D+00	(3.20)
a_4^ρ (δ_4^ρ)	0.345546671885201D+00	(4.20)
a_5^ρ (δ_5^ρ)	0.152483050063800D-02	(5.00)
a_1^F	-1.000000000000000	
a_2^F	-0.797773363680000D-04	

9. Appendix

9.1. Analytical form and parameters of EAM potentials

The analytical form of EAM potentials in this work is similar to the form developed by Mendelev et al. (33) and Ackland et al. (35) for iron and is expressed as:

$$E\left(\mathbf{r_1},\ldots,\mathbf{r_N}\right) = \sum_{i=1}^{N}\left[\sum_{j>i}^{N}\Phi(r_{ij}) + F\left(\rho_i\right)\right], \quad (1)$$

$$\Phi\left(x\right) = \sum_{i=1}^{n^{\Phi}} a_i^{\Phi}\left(\delta_i^{\Phi}-x\right)^3\Theta\left(\delta_i^{\Phi}-x\right), \quad (2)$$

$$\rho\left(x\right) = \sum_{i=1}^{n^{\rho}} a_i^{\rho}\left(\delta_i^{\rho}-x\right)^3\Theta\left(\delta_i^{\rho}-x\right), \quad (3)$$

$$F\left(x\right) = a_1^F\sqrt{x}+a_2^F x^2, \quad (4)$$

where Φ, ρ and F are the functions describing pairwise interatomic interactions, the effective electron density, and the embedded function, respectively. Here, $\Theta(x)$ is the Heaviside step function, which is equal to one for $x \geq 0$ and zero otherwise. In the case of the $a_2^F = 0$ and $a_1^F = -1$ we obtain the second moment tight binding approximation (17; 30; 29; 60; 61; 19). In the present study the parameter a_1^F was set to -1.

Tables 2 and 3 present the values of the parameters for potentials EAM2 and EAM3, respectively.

9.2. Fitting procedure: database

The database contains experimental and *ab initio* observables. The experimental observables such as lattice parameters and cohesive energies of the FCC/BCC structures and elastic constants C11, C12 and C44 are completed with different minima configurations (self-interstitials and vacancies). The force matching method is used on random iron configurations far from equilibrium.

The mono-interstitial with different orientations ($\langle 110\rangle$, $\langle 111\rangle$, $\langle 100\rangle$, octahedral and tetrahedral) and the mono-vacancy are included in the database as well as the di-interstitials $I_2^{\langle 110\rangle}$ and I_2^{gao}. These *ab initio* calculations were performed within the Density Functional Theory (DFT) framework using the SIESTA code, i.e. using the pseudopotential approximation and localized basis sets − made of 10 localized functions. The defect calculations were performed using the supercell approximation keeping the cell geometry fixed to the bulk equilibrium geometry and relaxing the atomic positions. The $6\times6\times6$, $4\times4\times4$ and $3\times3\times3$ shifted

k-point grids were used in the 54, 128 and 250 atom cells, respectively. The Hermite-Gauss scheme for electronic density of state broadening was used with a smearing of 0.3 eV and the residual forces were smaller than 0.01 eV/A. The standard Perdew-Burke-Ernzerhof Generalized Gradient Approximation (GGA) was used for exchange-correlation functional.

The *ab initio* forces acting on the atoms in the liquid or random state configurations. All the random configurations were generated using the Ackland-Mendelev potential for iron. This liquid was propagated using molecular dynamics at temperature of 4000 K over one million molecular dynamics steps (the integration step is set to 1 fs). From this molecular dynamics trajectory, we extracted one liquid configuration each 50 ps. The time interval between snapshots was large enough to avoid correlation due to the molecular dynamics propagation. Finally, all 20 random configurations were used as input for the *ab initio* calculations. The positions of atoms were frozen and only the atomic forces acting on each atom in each liquid configuration are computed. The *ab initio* calculations were performed using SIESTA GGA with the same pseudo potential and basis sets used for defect calculations.

References

References

[1] S. J. Zinkle, Challenges in developing materials for fusion technology - past, present and future, Fusion Sci. Technol. 64 (2) (2013) 65.

[2] R. Klueh, A. Nelson, Ferritic/martensitic steels for next-generation reactors, J. Nucl. Mater. 371 (1-3) (2007) 37.

[3] B. C. Masters, Dislocation loops in irradiated iron, Philos. Mag. 11 (113) (1965) 881.

[4] Z. Yao, M. L. Jenkins, M. Hernández-Mayoral, M. A. Kirk, The temperature dependence of heavy-ion damage in iron: A microstructural transition at elevated temperatures, Philos. Mag. 90 (35) (2010) 4623.

[5] M. E. Downey, B. L. Eyre, Neutron irradiation damage in molybdenum, Philos. Mag. 11 (109) (1965) 53.

[6] M.-C. Marinica, F. Willaime, J.-P. Crocombette, Irradiation-induced formation of nanocrystallites with $c15$ laves phase structure in bcc iron, Phys. Rev. Lett. 108 (2012) 025501.

[7] J. Dérès, L. Proville, M.-C. Marinica, Dislocation depinning from nano-sized irradiation defects in a bcc iron model, Acta Mater. 99 (2015) 99.

[8] L. Dézerald, M.-C. Marinica, L. Ventelon, D. Rodney, F. Willaime, Stability of self-interstitial clusters with C15 Laves phase structure in iron, J. Nucl. Mater. 449 (1-3) (2014) 219.

[9] A. Kaczmarowski, S. Yang, I. Szlufarska, D. Morgan, Genetic algorithm optimization of defect clusters in crystalline materials, Comput. Mater. Sci. 98 (2015) 234.

[10] R. Alexander, M.-C. Marinica, L. Proville, F. Willaime, K. Arakawa, M. R. Gilbert, S. L. Dudarev, Ab initio scaling laws for the formation energy of nanosized interstitial defect clusters in iron, tungsten, and vanadium, Phys. Rev. B 94 (2) (2016) 024103.

[11] A. Chartier, M. C. Marinica, Rearrangement of interstitial defects in alpha-Fe under extreme condition, Acta Materialia 180 (2019) 141–148.

[12] J. Byggmästar, F. Granberg, A. E. Sand, A. Pirttikoski, R. Alexander, M.-C. Marinica, K. Nordlund, Collision cascades overlapping with self-interstitial defect clusters in Fe and W, J. Phys.: Condens. Matter 31 (24) (2019) 245402.

[13] N. Mousseau, L. K. Béland, P. Brommer, J.-F. Joly, F. El-Mellouhi, E. Machado-Charry, M.-C. Marinica, P. Pochet, The Activation-Relaxation Technique: ART Nouveau and Kinetic ART, J. At. Mol. Opt. Phys. 2012 (2012) 1.

[14] T. D. Swinburne, D. Perez, Self-optimized construction of transition rate matrices from accelerated atomistic simulations with Bayesian uncertainty quantification, Phys. Rev. Materials 2 (5) (2018) 053802.

[15] Y. Zhang, X.-M. Bai, M. R. Tonks, S. B. Biner, Formation of prismatic loops from C15 Laves phase interstitial clusters in body-centered cubic iron, Scripta Mater. 98 (2015) 5.

[16] J. Byggmästar, F. Granberg, Dynamical stability of radiation-induced C15 clusters in iron, Journal of Nuclear Materials 528 (2020) 151893.

[17] R. P. Gupta, Lattice relaxation at a metal surface, Phys. Rev. B 23 (1981) 6265–6270.

[18] G. J. Ackland, R. Thetford, An improved N-body semi-empirical model for body-centred cubic transition metals, Philos. Mag. A 56 (1) (1987) 15.

[19] V. Rosato, M. Guillope, B. Legrand, Thermodynamical and structural properties of f.c.c. transition metals using a simple tight-binding model, Philos. Mag. A 59 (2) (1989) 321–336.

[20] M. S. Daw, M. I. Baskes, Embedded-atom method: Derivation and application to impurities, surfaces, and other defects in metals, Phys. Rev. B 29 (1984) 6443–6453.

[21] M. S. Daw, S. M. Foiles, M. I. Baskes, The embedded-atom method: a review of theory and applications, Mater. Sci. Reports 9 (7-8) (1993) 251.

[22] M. I. Baskes, Modified embedded-atom potentials for cubic materials and impurities, Phys. Rev. B 46 (5) (1992) 2727.

[23] J. S. Luo, B. Legrand, Multilayer relaxation at surfaces of body-centered-cubic transition metals, Phys. Rev. B 38 (1988) 1728–1733.

[24] D. G. Pettifor, New many-body potential for the bond order, Phys. Rev. Lett. 63 (22) (1989) 2480.

[25] D. G. Pettifor, Bonding and structure of molecules and solids, Oxford University Press, Oxford, 1996.

[26] A. P. Horsfield, A. M. Bratkovsky, M. Fearn, D. G. Pettifor, M. Aoki, Bond-order potentials: Theory and implementation, Phys. Rev. B 53 (19) (1996) 12694.

[27] M. C. Desjonquères, D. Spanjaard, Concepts in Surface Physics, Springer-Verlag, New York, 1993.

[28] M. W. Zimmmerman, Interatomic forces in condensed matter., Oxford University Press, Oxford, 2003.

[29] M. W. Finnis, J. E. Sinclair, A simple empirical N-Body potential for transition metals, Philos. Mag. A 50 (1984) 45.

[30] A. P. Sutton, J. Chen, Long-range Finnis-Sinclair potentials, Phil. Mag. Lett. 61 (1990) 139–146.

[31] G. J. Ackland, D. J. Bacon, A. F. Calder, T. Harry, Computer simulation of point defect properties in dilute FeCu alloy using a many-body interatomic potential, Philos. Mag. A 75 (3) (1997) 713.

[32] F. Ercolessi, J. B. Adams, Interatomic Potentials from First-Principles Calculations: The Force-Matching Method, Europhys. Lett. 26 (1994) 583.

[33] M. I. Mendelev, D. J. Srolovitz, G. J. Ackland, D. Y. Sun, M. Asta, Developement of new interatomic potentials appropriate for crystalline and liquid iron, Philos. Mag. 83 (2003) 3977.

[34] P. A. Gordon, T. Neeraj, M. I. Mendelev, Screw dislocation mobility in bcc metals: a refined potential description for α-Fe, Philos. Mag. 91 (30) (2011) 3931.

[35] G. J. Ackland, M. I. Mendelev, D. J. Srolovitz, S. Han, A. V. Barashev, Development of an interatomic potential for phosphorus impurities in α-iron, J. Phys.: Condens. Matter 16 (27) (2004) S2629.

[36] L. Malerba, M.-C. Marinica, N. Anento, C. Björkas, H. Nguyen, C. Domain, F. Djurabekova, P. Olsson, K. Nordlund, A. Serra, D. Terentyev, F. Willaime, C. S. Becquart, Comparison of empirical interatomic potentials for iron applied to radiation damage studies, J. Nucl. Mater. 406 (1) (2010) 19.

[37] L. Proville, D. Rodney, M.-C. Marinica, Quantum effect on thermally activated glide of dislocations, Nat. Mater. 11 (10) (2012) 845.

[38] J. Behler, M. Parrinello, Generalized neural-network representation of high-dimensional potential-energy surfaces, Phys. Rev. Lett. 98 (2007) 146401.

[39] A. P. Bartók, M. C. Payne, R. Kondor, G. Csányi, Gaussian approximation potentials: The accuracy of quantum mechanics, without the electrons, Phys. Rev. Lett. 104 (2010) 136403.

[40] J. Behler, Atom-centered symmetry functions for constructing high-dimensional neural network potentials, J. Chem. Phys. 134 (7) (2011) 074106.

[41] A. Thompson, L. Swiler, C. Trott, S. Foiles, G. Tucker, Spectral neighbor analysis method for automated generation of quantum-accurate interatomic potentials, Journal of Computational Physics 285 (2015) 316 – 330.

[42] M. A. Wood, A. P. Thompson, Quantum-accurate molecular dynamics potential for tungsten, arXiv:1702.07042v1 [physics.comp-ph].

[43] M. A. Wood, A. P. Thompson, Extending the accuracy of the SNAP interatomic potential form, Journal of Chemical Physics 148 (24).

[44] A. P. Bartók, J. Kermode, N. Bernstein, G. Csányi, Machine learning a general-purpose interatomic potential for silicon, Phys. Rev. X 8 (2018) 041048.

[45] A. M. Goryaeva, J.-B. Maillet, M.-C. Marinica, Towards better efficiency of interatomic linear machine learning potentials, Computational Materials Science 166 (2019) 200 – 209.

[46] D. Dragoni, T. D. Daff, G. Csányi, N. Marzari, Achieving dft accuracy with a machine-learning interatomic potential: Thermomechanics and defects in bcc ferromagnetic iron, Phys. Rev. Materials 2 (2018) 013808.

[47] W. J. Szlachta, A. P. Bartók, G. Csányi, Accuracy and transferability of gaussian approximation potential models for tungsten, Phys. Rev. B 90 (2014) 104108.

[48] C.-C. Fu, J. D. Torre, F. Willaime, J.-L. Bocquet, A. Barbu, Multiscale modelling of defect kinetics in irradiated iron, Nat. Mater. 4 (2005) 68.

[49] D. A. Terentyev, T. P. C. Klaver, P. Olsson, M.-C. Marinica, F. Willaime, C. Domain, L. Malerba, Self-trapped interstitial-type defects in iron, Phys. Rev. Lett. 100 (2008) 145503.

[50] M.-C. Marinica, F. Willaime, N. Mousseau, Energy landscape of small clusters of self-interstitial dumbbells in iron, Phys. Rev. B 83 (2011) 094119.

[51] F. Gao, D. J. Bacon, Y. N. Osetsky, P. E. J. Flewitt, T. A. Lewis, Properties and evolution of sessile interstitial clusters produced by displacement cascades in α-iron, J. Nucl. Mater. 276 (1-3) (2000) 213.

[52] L. Ventelon, F. Willaime, Core structure and Peierls potential of screw dislocations in α-Fe from first principles: cluster versus dipole approaches, J. Computer-Aided Mat. Design 14 (2007) 85–94.

[53] C. Domain, C. S. Becquart, Ab initio calculations of defects in Fe and dilute Fe-Cu alloys, Phys. Rev. B 65 (2001) 024103.

[54] C.-C. Fu, F. Willaime, P. Ordejón, Stability and mobility of mono- and di-interstitials in α-Fe, Phys. Rev. Lett. 92 (2004) 175503.

[55] P. Ehrhart, K. H. Robrock, H. R. Schober, Chapter 1 - basic defects in metals, in: R. Johnson, A. Orlov (Eds.), Physics of Radiation Effects in Crystals, Vol. 13 of Modern Problems in Condensed Matter Sciences, Elsevier, 1986, p. 3.

[56] S. L. Dudarev, P. M. Derlet, Magnetic interatomic potential for molecular dynamics simulations, J. Phys. Condens. Mat. 17 (44) (2005) 7097.

[57] M.-C. Marinica, L. Ventelon, M. R. Gilbert, L. Proville, S. L. Dudarev, J. Marian, G. Bencteux, F. Willaime, Interatomic potentials for modelling radiation defects and dislocations in tungsten, J. Phys.: Cond. Mater. 25 (39) (2013) 395502.

[58] D. J. Wales, Energy Landscapes., Cambridge University Press, Cambridge, 2004.

[59] T. D. Swinburne, M.-C. Marinica, Unsupervised calculation of free energy barriers in large crystalline systems, Phys. Rev. Lett. 120 (13) (2018) 135503.

[60] J. Friedel, The Physics of Metals 1 (1969) 494.

[61] F. Cyrot-Lackmann, Thése de Doctorat, Université Paris-Sud.